Journal of Geodesy (2025) 99:89
https://doi.org/10.1007/s00190-025-02010-z

ORIGINAL ARTICLE

Grazing-angle ionospheric delays observed during the GNSS-R PRETTY mission

Mario Moreno[1,4] · **Maximilian Semmling**[1] · **Florian Zus**[2] · **Georges Stienne**[3] · **Andreas Dielacher**[5,6] · **Mainul Hoque**[1] · **Jens Wickert**[2,4] · **Hossein Nahavandchi**[7]

Received: 21 November 2024 / Accepted: 30 September 2025 / Published online: 25 October 2025

Abstract

Spaceborne GNSS reflectometry (GNSS-R) has emerged as a valuable technique for surface and atmospheric remote sensing, particularly under grazing-angle geometries where atmospheric effects are amplified. Single-frequency missions such as ESA passive REflecTomeTry and dosimetrY (PRETTY) rely on model-based corrections to account for ionospheric and tropospheric delays. In this study, we exploit PRETTY's capabilities to perform observations down to 1 degree (at the specular point) to investigate ionospheric effects at very low angles. We analyze six GNSS-R events recorded over the North Polar region in July 2024, focusing on the estimation of the relative ionospheric delay using code delay observations. Comparisons with model-based ionospheric delays from NEDM2020, NeQuick, and IRI show close agreement, with NEDM2020 consistently exhibiting the lowest residual differences, ranging from 1.28 to 4.39 m across all events. This supports the ability of GNSS-R code delay observables to capture the first-order ionospheric delay with reasonable fidelity. Uncertainty analysis reveals that the observed delay fitting process dominates the overall error budget, with additional contributions from tropospheric correction and surface height uncertainty. Furthermore, inversion of the fitted delays using the Chapman layer model yields plausible F-layer parameters, with peak heights ranging from 307 to 367 km and a mean delay RMSE of approximately 1.2 m (~ 4 TECU). Comparisons with ionosonde and EISCAT measurements show differences within ± 15 km. These results demonstrate the potential of single-frequency GNSS-R missions for retrieving ionospheric structure, particularly in remote regions where conventional techniques are limited or unavailable.

Keywords PRETTY · GNSS reflectometry · Ionospheric delay · Grazing angles · Code delay · NEDM2020 model

1 Introduction

The increasing use of CubeSats in a wide range of applications, including Earth observation and atmospheric science, reflects the growing versatility, reduced cost, and adaptability of these small satellite platforms. CubeSats are now contributing to advanced remote sensing techniques, including Global Navigation Satellite Systems Reflectometry (GNSS-R), which has demonstrated significant potential for monitoring Earth's surface and atmospheric properties. GNSS-R leverages signals from GNSS, reflected off Earth's surface, to derive information on surface characteristics and atmospheric conditions. Beyond its well-established use in sea surface altimetry (Cardellach et al. 2020) and sea ice monitoring (Alonso-Arroyo et al., 2016; Cartwright et al. 2019), GNSS-R is also emerging as a valuable technique for ionospheric and tropospheric studies, particularly in spaceborne Low Earth Orbit (LEO) platforms, enabling applications such

✉ Mario Moreno
mario.moreno@dlr.de

[1] Deutsches Zentrum Für Luft- und Raumfahrt, Institut für Solar-Terrestrische Physik (DLR-SO), Neustrelitz, Germany

[2] Deutsches GeoForschungsZentrum (GFZ), Potsdam, Germany

[3] Laboratoire d'Informatique, Signal et Image de la Côte d'Opale (LISIC), Université Littoral Côte d'Opale (ULCO), Calais, France

[4] Technische Universität Berlin (TUB), Berlin, Germany

[5] Beyond Gravity Austria GmbH (BGA), Vienna, Austria

[6] Technische Universität Graz (TUG), Graz, Austria

[7] Norwegian University of Science and Technology (NTNU), Trondheim, Norway

as total electron content (TEC) estimation (Ren et al. 2022) or water vapor retrievals (Wang 2023b).

A critical atmospheric effect that needs to be accounted for spaceborne GNSS-R missions is ionospheric delay. As the GNSS signals traverse through the ionosphere, the TEC induces delays that affect the direct (GNSS-to-LEO), incident (GNSS-to-specular point), and reflected (specular point-to-LEO) paths. This effect is especially pronounced at lower elevation angles, which are typical of spaceborne GNSS-R observations under grazing geometries.

The importance of accounting for ionospheric delays in spaceborne GNSS-R has been highlighted in earlier works. Prior to the Cyclone Global Navigation Satellite System—-CYGNSS mission (Ruf et al. 2013a, b) launched in 2016, Xing et al. (2015) conducted simulations using the International Reference Ionosphere (IRI) Model (Bilitza et al. 2022) to quantify ionospheric delay effects on the Delay Doppler Map (DDM) observables. Their results indicated that the ionospheric delay is inversely proportional to satellite elevation and can reach up to 30 m for elevations as low as 30°. Based on the GNSS-R geometry considered in that study, the relative ionospheric delay was found to be primarily influenced by the contributions of the incident and reflected signal paths.

In another study Camps et al. (2016), used data from the single-frequency TechDemoSat-1 (TDS–1) mission (Unwin et al. 2016) and showed that at 55° elevation, ionospheric delays can range between 1 and 3 TECU (0.16–0.5 m in L1), with signal-to-noise ratio (SNR) fluctuations driven by ionospheric scintillation, especially within ± 20° latitude of the geomagnetic equator. However, neither of these studies addressed ionospheric effects at grazing geometries where atmospheric effects become even more pronounced and complex.

Recent developments in GNSS-R spaceborne missions have advanced the ionospheric corrections and retrievals, particularly through the use of dual-frequency observations Wang and Morton, (2022). used dual-frequency coherent GNSS-R observations from Spire CubeSats to retrieve relative TEC over sea ice and calm oceans at grazing angles, demonstrating high precision for ionospheric disturbance monitoring. However, these techniques rely on carrier phase observables and are limited in rough ocean regions where coherent reflections are not sustained.

To address these limitations Wang (2023a), introduced a novel approach to estimate ionospheric delay using single-frequency GNSS-R pseudorange measurements, especially leveraging the wideband GPS L5 and Galileo E5 signals. This method aims to extract ionospheric TEC from the residual of modeled pseudorange, correcting for geometric range, clock biases, surface height, and tropospheric delays. Wang presented that with proper corrections, pseudorange-based TEC retrieval can achieve sub-meter precision (2–3.4 TECU) for GPS L5 under moderate sea surface conditions. However, the study used simulations and L1/L2 data due to the lack of actual L5/E5 data at the time.

The ESA PRETTY (Passive Reflectometry and Dosimetry) CubeSat mission (Dielacher et al. 2022), launched in October 2023, represents a novel approach to GNSS-R by utilizing the L5/E5 signal bands for altimetric applications at grazing angles. Developed by Beyond Gravity Austria GmbH, Graz University of Technology, and Seibersdorf Laboratories, PRETTY aims to measure sea surface height and related geophysical parameters such as significant wave height, sea ice type, and concentration, primarily in polar regions, using single-frequency observations. Due to its reliance on a single frequency, PRETTY applies model-based corrections to compensate for atmospheric delays.

PRETTY's onboard software supports observations at very low-elevation angles—down to 0.01°—allowing precise analysis of atmospheric effects on reflected signals. The satellite can operate in both clean replica GNSS-R (cGNSS-R) and interferometric GNSS-R (iGNSS-R) modes. The cGNSS-R mode uses a locally generated reference signal for correlation, while the iGNSS-R relies on the direct signal received by the satellite as the reference for interferometric processing (Cardellach et al. 2018) .

PRETTY mission also provides both code delay and phase observables, offering valuable opportunities for atmospheric and geophysical studies. However, at the time of this study, the phase data and the iGNSS-R observations are still undergoing validation and verification by the mission team and are not yet available for scientific analysis.

In this study, we focus on the estimation of ionospheric delay using PRETTY code delay observations. Previous GNSS-R missions have focused either on correlation maps over delay doppler maps in near-nadir geometry with incidence at the reflection point below 60° (e.g., TDS-1, CYGNSS) or on a single coherent correlator sampling in grazing geometries with respective incidence angle above 60°, as in the spire constellation. The PRETTY mission provides correlation maps highly resolved in delay, even under grazing geometries. It allows us to study atmospheric effects using code delay observations in the grazing-angle regimes where atmospheric effects are especially variable.

We analyze six events collected over the Northern Polar region during July 2024 and estimate the 'relative' ionospheric delay—here defined as the difference in ionospheric delay between the reflected and direct signal paths in the GNSS-R geometry. Based on these estimations from PRETTY, we assess the feasibility of retrieving the vertical ionospheric structure by fitting a Chapman layer model to the observed delay profiles, aiming to derive key F-layer parameters such as the peak electron density, peak height, and scale height.

This paper is structured as follows: Sect. 2 details the methodology, describing the data used and the approach to compute relative ionospheric and tropospheric delays. Section 3 presents the results, including the delay maps, the correction and estimation of relative ionospheric delay, and Chapman layer parameter inversion. Finally, Sect. 4 concludes with key takeaways and outlines directions for future work, including opportunities enabled by using PRETTY data.

2 Data and methodology

2.1 GNSS-R PRETTY data

The ESA PRETTY CubeSat is a GNSS Reflectometry mission launched in October 2023 into a sun-synchronous polar LEO orbit at 560 km in height and an inclination of 97.66°. The mission's primary objective is to measure the sea surface height and other sea ice properties, particularly at grazing angles (Dielacher et al. 2022). PRETTY is a pioneering mission in the field of GNSS reflectometry, utilizing E5/L5 signal bands from the European Galileo and U.S. GPS satellites. Its system is highly adaptable and capable of conducting observations across a wide range of elevation angles, from 30° down to as low as 0.01°, offering flexibility for diverse data acquisition scenarios. As of September 2024, the PRETTY mission has conducted multiple measurements across various locations, with a primary focus on the North Polar region. These observations have been carried out using signals from both the GPS and Galileo constellations, covering a wide range of grazing-angle elevations. The distribution of reflection point tracks recorded by PRETTY is shown in Fig. 1.

A total of six events were selected for this study. These observations represent the cases with the highest signal-to-noise ratio (SNR) levels, computed as the peak signal power relative to the noise level in decibels (dB), and featuring elevation grazing angles down to 1° or lower. The selected events also cover different levels of solar activity, as indicated by the variability in the solar flux index F10.7.

Table 1 summarizes the key information for each selected event, including the date, GNSS constellation and PRN, observation start time in UTC, elevation range, duration of the analyzed event, SNR range, and the corresponding F10.7 index value (in solar flux units, sfu), obtained from the National Research Council and Natural Resources Canada.

In Fig. 2, the left panel displays the locations of the selected events, color-coded by the date of recording, with markers indicating the GNSS constellation, stars for Galileo, and circles for GPS. The right panel illustrates the corresponding SNR levels for each event.

2.2 Delay maps and code delay

The raw data from the PRETTY receiver is recorded as complex waveforms sampled at 1 ms intervals. From this raw data, the next-level data product, known as the Delay Map (DM) observable, is derived. The DM is a time-delay representation of the reflected GNSS signals, offering insight into how these signals arrive at different delays relative to the direct signals, after bouncing off the reflecting surface. In the DM, the y-axis shows the signal delay, representing the excess path length of the reflected signal relative to the direct signal, while the signal intensity is color-coded. The DM has been employed in GNSS-R for applications such as ice sheet altimetry, as demonstrated in Rius et al. (2017) using TDS–1 data.

The PRETTY DM is generated during postprocessing in two steps. First, the signal is coherently integrated every 20 ms. This is followed by an incoherent integration every second, allowing for longer integration periods since it does not depend on maintaining phase information. The location of the peak intensity on the y-axis for each power waveform in the DM represents the relative observed code delay. The PRETTY DMs are configured into 200 taps along the delay axis, with each tap corresponding to a resolution of 7.8071 m. This offers a finer delay range resolution compared to the 37.5 m resolution of the TDS-1 mission (Foti et al. 2015) and the 25 m resolution of the CYGNSS mission (Ruf et al. 2013a, b).

The ability to observe GNSS-R signals down to 1° of elevation is a key advantage of the PRETTY mission. At such grazing angles, the reflected signal paths traverse longer atmospheric segments, significantly amplifying atmospheric delay signatures, particularly those related to ionospheric and tropospheric effects. This geometry enables greater sensitivity to the vertical structure of the atmosphere, especially the ionosphere. Moreover, surface roughness effects become less dominant at very low elevations, favoring conditions for coherent reflections, especially over calm ocean or ice surfaces. These coherent returns enhance the detectability of systematic delay trends.

As illustrated in the Delay Maps in Fig. 3, when the elevation falls below approximately 4°, the relative code delay exhibits a marked drift (i.e., a nonlinear increase), continuing until it reaches the lowest elevation of ~ 1°. This delay curvature is indicative of the influence of atmospheric refraction and dispersion at low-elevation angles. These features would remain undetectable at higher elevation regimes (e.g., > 5°).

As shown in Table 1, all observations correspond to setting events (i.e., decreasing elevation angles). The events on 06 July and 16 July extend down to 1° in elevation (at the specular point location), whereas the events from 25 July onward reach as low as 0.01°. However, in the Delay Maps from these latter events, it becomes evident that below 1° of

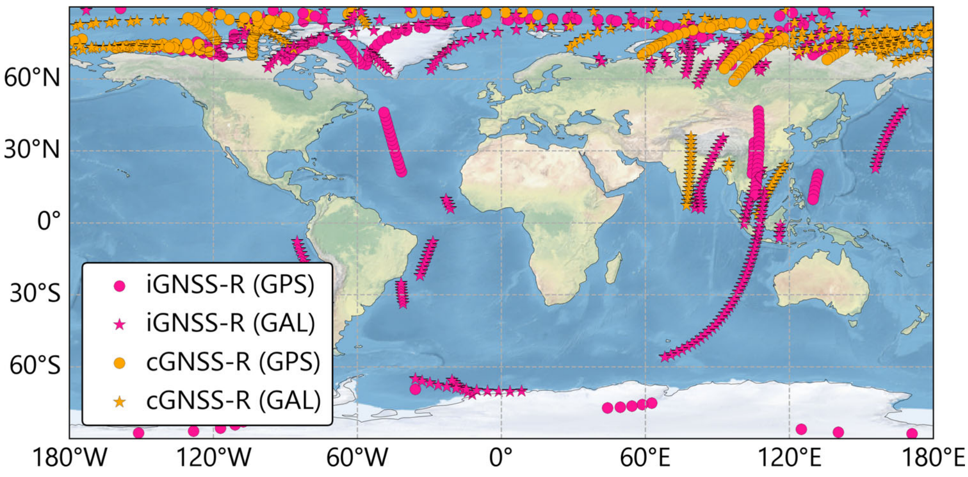

Fig. 1 Location of reflection point tracks recorded by PRETTY as of September 2024 using cGNSS-R (orange) or iGNSS-R (magenta) and Galileo (stars) or GPS (dots) system

Table 1 Overview of the selected events, summarizing key observational parameters

Date	GNSS-PRN	UTC	Ele. [deg]	Duration [mm:ss]	SNR [dB]	F10.7 [sfu]
2024/07/06	GAL–7	01:35:48	7–1	03:09	5.10–9.44	169.9
2024/07/16	GAL–7	00:55:51	10–1	04:12	5.25–9.11	242.4
2024/07/25	GPS–4	05:05:53	9–0.01	03:58	6.31–12.09	172.0
2024/07/27	GPS–8	04:55:51	11–0.01	06:34	5.96–10.26	186.7
2024/07/28	GPS–8	04:50:52	13–0.01	07:21	5.61–11.59	216.6
2024/07/29	GPS–8	04:45:50	15–0.01	08:10	5.88–12.11	224.2

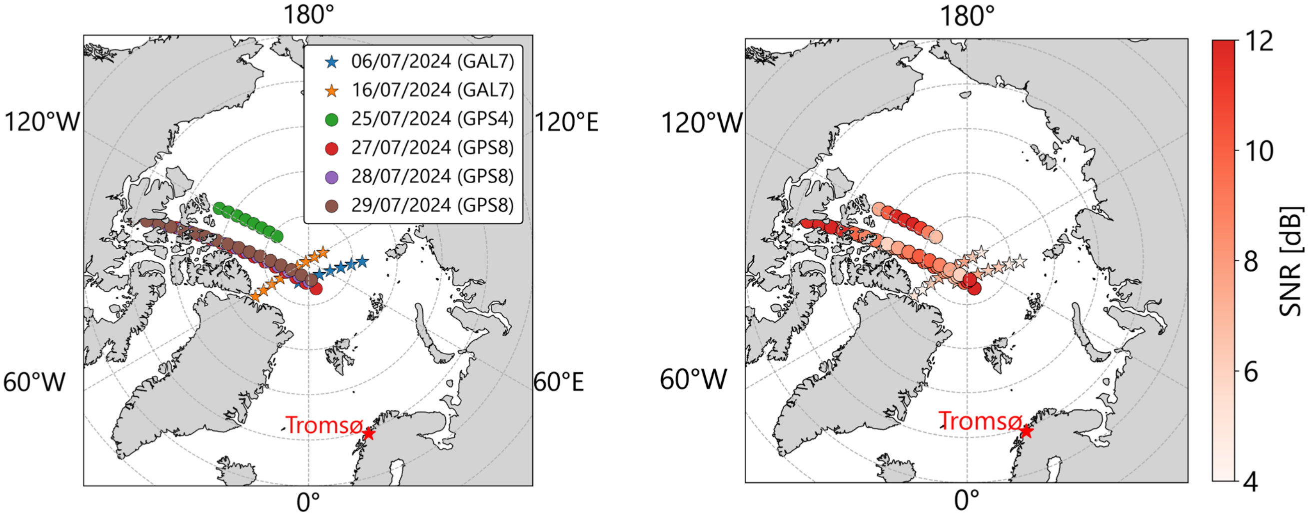

Fig. 2 Left: Specular points tracks, color-coded by date (stars: Galileo events, and circles: GPS events). Right: SNR levels of the selected events. The Tromsø ionosonde (EISCAT station) is located near the observed events

elevation, the relative code delay becomes noisier, and the direct signal delay starts to appear with increased intensity, making it more challenging to identify the relative code delay peak. As a result, all event samples have been truncated at the 1° elevation limit to ensure reliable analysis.

2.2.1 Code delay fitting

After the Delay Map is computed, the peak value of each power waveform is selected, and the corresponding code delay over time is extracted. In this step, it is necessary to remove outliers to ensure the consistency of the retrieved code delays. These outliers, such as signal power dissipation

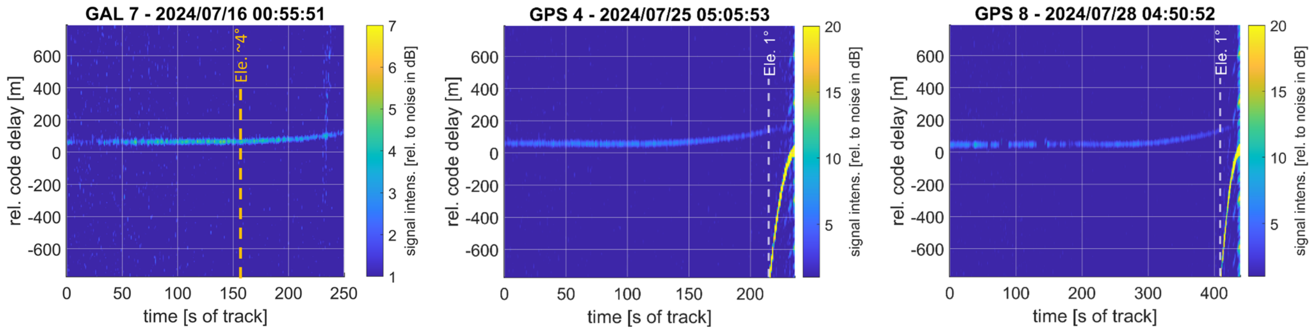

Fig. 3 PRETTY Delay Maps from 16, 25, and 28 July. The x-axis represents the seconds of the track, while the y-axis indicates the relative code delay converted to meters

in the DM, typically correspond to locations where the specular point crosses over land or rougher surfaces. For instance, in the DM from 28 July (Fig. 3, right), a power drop (or gap) is observed before the 100 s mark of the track, coinciding with the specular point crossing over Ellef Ringnes Island in Canada.

As presented in Fig. 4, the observed code delays exhibit a discrete stepped behavior, resulting from the delay resolution of the DMs. This quantization effect arises from the discrete tap configuration of the correlator, where each step corresponds to one delay bin (7.8071 m). To capture the underlying trend in the code delay, a fitting process is applied to the observations over the entire duration of each event. The model that best captures this trend is an exponential function of the form $y = a \cdot e^{bx} + c$, where y represents the code delay, and x is the independent variable, which in this case is time.

After the fitting process, the coefficient of determination R^2 is found to be close to 1, indicating a strong fit between the model and the observed code delay data. The uncertainty envelope associated with the fitting is derived using the 5th and 95th percentiles of the residuals, corresponding to the range within which 90% of the observations are expected to fall. The typical uncertainty range associated with the fitting is approximately ± 2.6 m.

Figure 4 presents the observed code delays along with the fitted curves and associated uncertainty bounds for the events on 16, 25, and 28 July.

2.3 Atmospheric delays

In GNSS-R, the relative path delay Δ_{p}, also referred to as the interferometric path delay, represents the difference between the reflected path delay, p_r (which includes both the incident and reflected rays), and the direct path delay, p_d (Cardellach et al. 2004). Considering the common sources of delay that affect GNSS signals, the relative delay can be expressed as follows:

$$\Delta_{\mathrm{p}} = \Delta_{\mathrm{p_{geo}}} + \Delta_{\mathrm{p_{trop}}} + \Delta_{\mathrm{p_{iono}}} + \Delta_{\mathrm{p_{rgh}}} + \Delta_{\mathrm{p_{instr}}} + n \qquad (1)$$

where $\Delta_{\mathrm{p_{geo}}}$ represent the geometrical delay, $\Delta_{\mathrm{p_{trop}}}$ accounts for the relative path delay caused by tropospheric refraction, and $\Delta_{\mathrm{p_{iono}}}$ corresponds to the relative ionospheric path delay. Additionally, there is an induced bias due to surface roughness, denoted as $\Delta_{\mathrm{p_{rgh}}}$, while instrumental and unmodeled errors are represented by $\Delta_{\mathrm{p_{instr}}}$ and n, respectively.

Due to the geometry of spaceborne GNSS-R at grazing angles, the signals traverse a longer path through the atmosphere, resulting in a larger atmospheric impact. In this study, we focus on correcting and analyzing the two major atmospheric contributions: the relative tropospheric delay $\Delta_{\mathrm{p_{trop}}}$ and the relative ionospheric (group) delay $\Delta_{\mathrm{p_{iono}}}$. Since PRETTY is a single-frequency (E5/L5) mission, it relies on atmospheric models to account for the delays introduced along the direct, incident, and reflected signal paths. Corrections for geometric and instrumental delays are handled by the mission's onboard processing. The following section describes the methodologies used to compute the model-based tropospheric delay applied for correction, as well as the ionospheric delays used for comparison with the estimates derived from the observations.

2.3.1 Model-based relative ionospheric delay

The ionosphere, a layer of the upper atmosphere composed of charged particles, induces delays in GNSS signals that depend on the TEC (Morton et al. 2020). The slant TEC (sTEC) refers to the total number of electrons per square meter (electron density) along the signal path between a GNSS satellite and a receiver, and it is commonly measured in total electron content uits (TECU), where one TECU is equivalent to 10^{16} electrons per square meter.

In this study, the model-based sTEC along each ray path is computed using three different models: the Neustrelitz electron density model—NEDM2020 (Hoque et al. 2022), the NeQuick model (Nava et al. 2008), and the International Reference Ionosphere Model (IRI) (Bilitza et al. 2022). These sTEC values are used to compute the modeled relative ionospheric delay. The resulting modeled delays are then

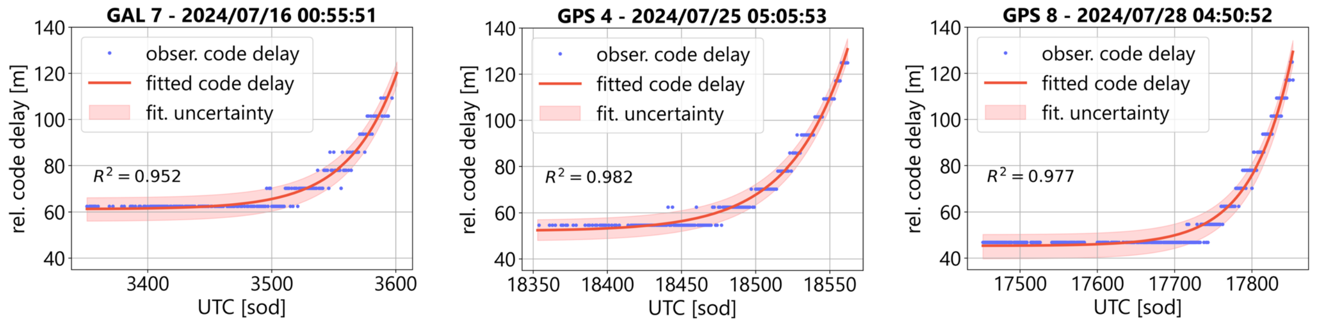

Fig. 4 Code delay observations with the exponential model fit, the coefficient of determination R^2, and its corresponding model uncertainty bounds

compared with the corresponding delay estimated from the PRETTY code delay observations.

The computation methodology follows the approach described by Moreno et al. (2023). The positions of the transmitter, receiver, and specular reflection point are obtained from PRETTY mission metadata, with the specular point already corrected for surface elevation using a digital elevation model integrated into the onboard system. Based on these positions, ray points are defined every 10 km along the ray paths of the direct (di), incident (in), and reflected (re) signals.

The electron density for each ray point is obtained from the respective three models. Both NEDM2020 and NeQuick provide electron density values directly for any 3D coordinate using inputs latitude, longitude, altitude, date, local time, and solar flux index. For the IRI model, electron density profiles are extracted from IRI-2016 and assembled into a 3D electron density field with a horizontal resolution of 2° × 2°. By integrating the electron density along each ray, the sTEC for the direct, incident, and reflected signals is obtained. The relative sTEC, $\Delta sTEC$, is then computed as $sTEC_{\mathrm{in}} + sTEC_{\mathrm{re}} - sTEC_{\mathrm{di}}$. Finally, the model-based relative ionospheric delay (in meters) can be determined as follows:

$$\Delta_{P_{iono}} = +\frac{40.3 * 10^{16}}{f^2}\Delta sTEC \qquad (2)$$

where f represents the GNSS carrier frequency in Hertz. For the PRETTY mission, this applies to the GPS L5 and Galileo E5 frequency bands, which operate at 1176.45 MHz.

2.3.2 Model-based relative tropospheric delay

The lowest layer of the Earth's atmosphere is the troposphere. The troposphere induces delays in GNSS signals that depend on variations in temperature, pressure, water vapor, and the relative positions of the transmitter and receiver (Hofmann-Wellenhof et al. 2012). To account for this effect, we retrieve model-based tropospheric corrections using ray-tracing techniques supported by numerical weather model data.

Specifically, we use the ERA5 reanalysis data (Hersbach et al. 2020) from the European Centre of Medium-Range Weather Forecasts (ECMWF), which provides atmospheric fields on 37 pressure levels at a horizontal resolution of 0.25° × 0.25°.

The computations are based on the point-to-point algorithm developed by Zus et al. (2012), which determines the signal path between transmitter and receiver and integrates the refractive index along that path to compute the optical length.

The process begins by computing the geometric path length P. Following the methodology described by Semmling et al. (2016), this path is first computed under the assumption of no atmospheric effects, using the known positions of the GNSS transmitter and the PRETTY receiver, thereby deriving an initial reflection point. The reflection point is then iteratively adjusted until the incident and reflected rays satisfy the law of reflection (i.e., the incidence angle equals the reflection angle). With the troposphere included, the new path length is computed and denoted as P_t. Finally, the ionospheric delay is added using the same reflection geometry, yielding the total atmospheric path length P_i. The total path length P_i can be expressed as:

$$P_{\mathrm{i}} = P + (P_{\mathrm{t}} - P) + (P_{\mathrm{i}} - P_{\mathrm{t}}) \qquad (3)$$

In this approach, $\Delta P_{\mathrm{t}} = (P_{\mathrm{t}} - P)$ represents the model-based relative tropospheric delay, and $\Delta P_{\mathrm{i}} = (P_{\mathrm{i}} - P_{\mathrm{t}})$ represents the relative ionospheric delay.

3 Results

3.1 Model-based atmospheric delays analysis

The model-based relative tropospheric and ionospheric delays are computed for each ray individually for all six selected events. Figure 5 illustrates three examples, showing the ionospheric delay (dashed lines) retrieved from the NEDM2020 model, and the modeled tropospheric delay

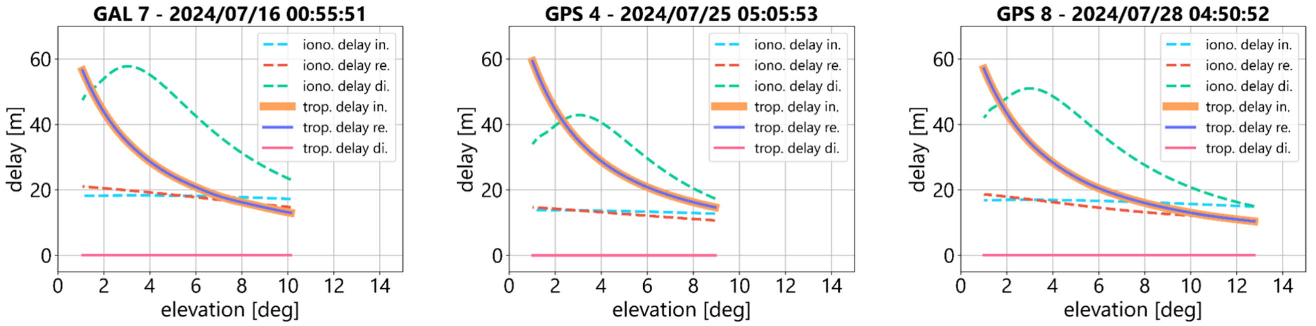

Fig. 5 Ionospheric (NEDM2020) and tropospheric delays for each ray –incident (in), reflected (re), and direct (di)– during the events on 16 July (GAL 7), 25 July (GPS 4), and 27 July (GPS 8)

(solid lines) for the events on 16, 25, and 28 July, color-coded to indicate the respective rays: incident, reflected, and direct. The event on 16 July corresponds to the day with the highest solar activity among the analyzed events (see Table 1).

Regarding the tropospheric delay in the three examples in Fig. 5, the contributions from the incident and reflected signals are similar, in agreement with the tropospheric correction approach presented by Fabra et al. (2011). Both exhibit an exponential increase as the elevation angle decreases, reaching values close to 60 m at an elevation of 1°. In contrast, the direct signal does not contribute within this elevation range. The ionospheric delay, however, shows more dynamic behavior across the three rays, with variations influenced by the solar activity level on each respective day. Ionospheric delay values are notably higher on days with increased solar flux. Moreover, the direct ray exhibits a pronounced increase in ionospheric delay across all days, peaking at around 3° of elevation in all cases, after which the delay contribution from the direct signal delay begins to decrease.

The model-based relative ionospheric and tropospheric delays are calculated as described in Sect. 2.3. When applying the modeled total atmospheric delay correction, i.e., the sum of the tropospheric and ionospheric delays, an offset remains between the observations and the model. This offset is primarily due to the configuration of the onboard code generator in the field-programmable gate array (FPGA) on the PRETTY satellite during clean replica observations. In this mode, processing begins by determining the direct signal delay to configure the code generator and compensate for any instrumental delays. Initially, the software estimates the delay error of the direct signal in an open-loop process by correlating it with a code delayed by an initial value, accounting for the discrepancy between the peak and estimated taps.

This initial compensation includes the geometric, ionospheric, and tropospheric delays at the first epoch of the observation. A correction using the first epoch of the total modeled atmospheric delay for the direct signal is applied to align the observed code delay with the modeled. Since the tropospheric delay is absent from the direct signal, the correction relies solely on the ionospheric delay. Applying this correction improves the alignment between the observations and the model, as shown in Fig. 6. The figure shows the modeled atmospheric delays alongside the observed code delay and the fitting curve. The orange curve represents the relative tropospheric delay, the blue curve is the relative ionospheric delay from NEDM2020, and the green curve is the total atmospheric delay. A clear trend agreement between the observed and modeled delays is evident, with both showing an exponential increase, particularly below 5° of elevation, indicating that the models reasonably capture the atmospheric delay dynamics.

3.2 Relative ionospheric delay estimation

To estimate the relative ionospheric delay, the modeled tropospheric delay is subtracted from the fitted code delay observations, as the geometric and instrumental delays are already corrected during onboard processing. This step isolates the ionospheric contribution by effectively removing the tropospheric influence. Focusing solely on the ionosphere enables a detailed examination of its impact on signal propagation and allows for direct comparison between the estimated and model-based relative ionospheric delays, helping to identify potential anomalies or discrepancies.

Figure 7 shows the relative ionospheric delay computed using the three different models: NEDM2020, NeQuick, and IRI. It also includes the estimated relative ionospheric delay (red curve), with associated uncertainty derived from model fitting errors and a tropospheric correction uncertainty of less than 1% (Zus et al. 2012). This uncertainty estimate for the tropospheric correction is based on statistical comparisons between weather model–based and GNSS-derived tropospheric delays. Therefore, it is a conservative estimate as it also includes the uncertainty of the GNSS estimates.

Overall, the relative ionospheric delay estimations align well with the selected models, with the NEDM2020 model

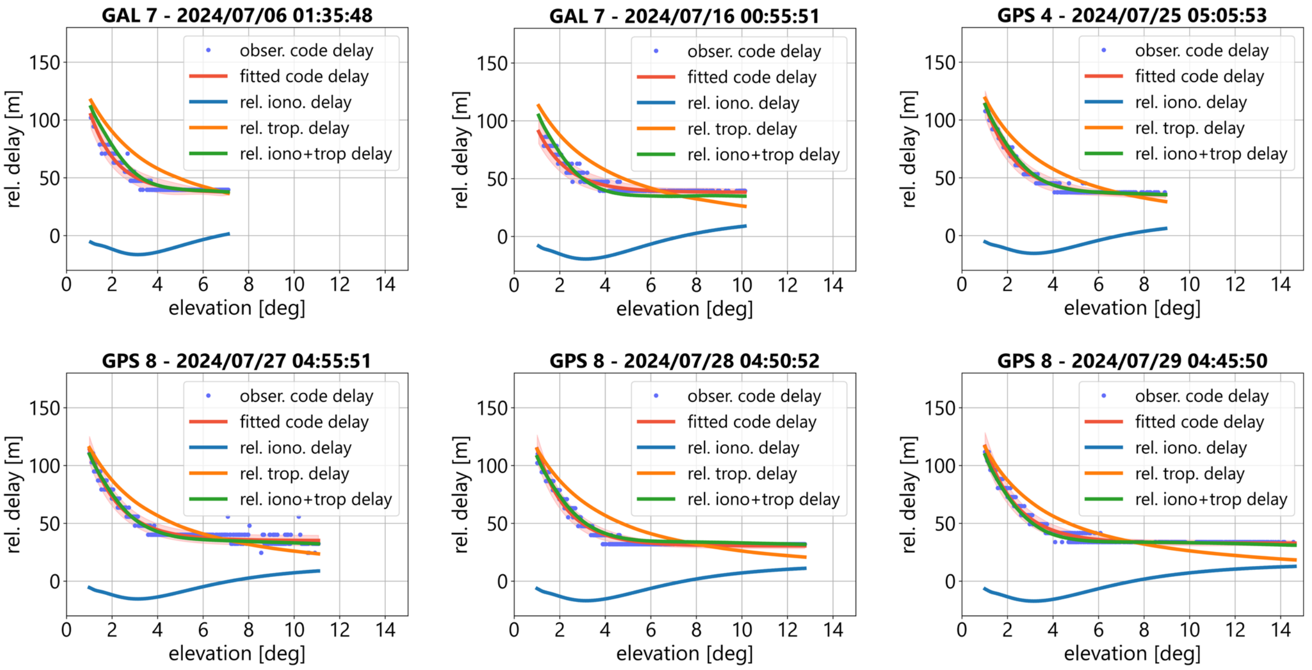

GAL 7 - 2024/07/06 01:35:48
GAL 7 - 2024/07/16 00:55:51
GPS 4 - 2024/07/25 05:05:53
GPS 8 - 2024/07/27 04:55:51
GPS 8 - 2024/07/28 04:50:52
GPS 8 - 2024/07/29 04:45:50

Fig. 6 Observed code delay with its fitting curve after applying the correction based on the first epoch total modeled atmospheric delay, along with the modeled relative ionospheric and tropospheric delays and their sum, representing the total modeled delay

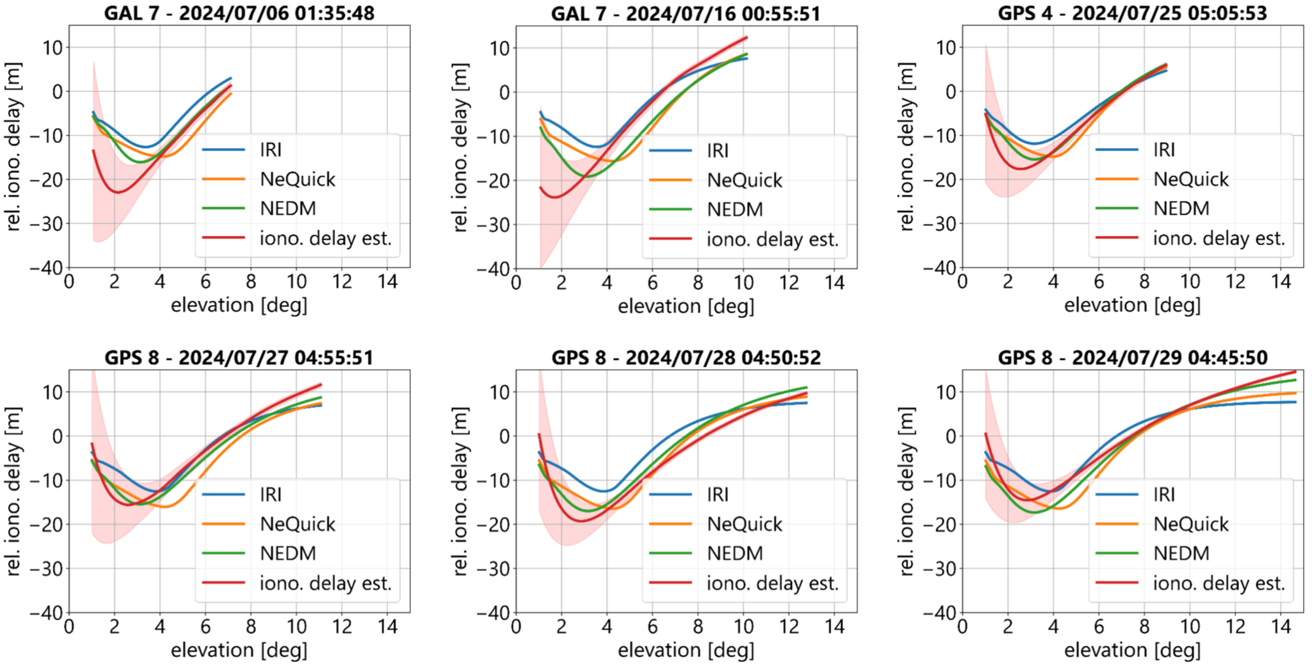

GAL 7 - 2024/07/06 01:35:48
GAL 7 - 2024/07/16 00:55:51
GPS 4 - 2024/07/25 05:05:53
GPS 8 - 2024/07/27 04:55:51
GPS 8 - 2024/07/28 04:50:52
GPS 8 - 2024/07/29 04:45:50

Fig. 7 Relative ionospheric delay computed using the IRI, NeQuick, and NEDM2020, along with the estimated relative ionospheric delay and its associated uncertainties from model fitting and tropospheric correction

Table 2 Residual standard deviations (in meters) between the GNSS-R estimated relative ionospheric delays and the corresponding values from each ionospheric model

Date	GNSS-PRN	UTC	NEDM2020	NeQuick	IRI
2024/07/06	GAL–7	01:35:48	3.75	5.49	3.82
2024/07/16	GAL–7	00:55:51	4.39	6.20	5.46
2024/07/25	GPS–4	05:05:53	1.79	2.82	4.86
2024/07/27	GPS–8	04:55:51	1.55	2.88	3.11
2024/07/28	GPS–8	04:50:52	1.39	2.42	3.27
2024/07/29	GPS–8	04:45:50	1.28	1.99	2.90

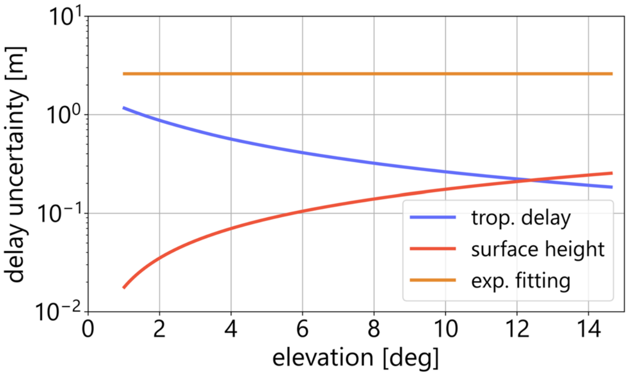

Fig. 8 Uncertainty contributions to the estimated relative ionospheric delay as a function of elevation angle

consistently exhibiting the lowest residual standard deviations across all events, as shown in Table 2. This close alignment suggests that NEDM2020 more accurately captures the slant delay variations observed under the specific conditions of each event. The reduced spread of residuals further supports that the estimation effectively retrieves the first-order ionospheric delay, which is directly proportional to the total electron content.

Notably, the largest deviations across all three models occur on 16 July, coinciding with the highest solar activity levels. This underscores the limitations of empirical models in capturing ionospheric variability under disturbed space weather conditions.

Figure 8 presents the uncertainties associated with the relative ionospheric delay estimations arising from the exponential fitting process, the model-based tropospheric delay correction, and including the reflecting surface height. Each contribution is evaluated as a function of elevation angle.

The uncertainty from the exponential fitting is approximately ± 2.6 m, as derived from the residual statistics during the curve fitting process. This value reflects the influence of PRETTY's delay map resolution and the discrete nature of peak tracking, which limits the precision in capturing continuous delay variations.

The uncertainty in the tropospheric delay correction is primarily based on ray-tracing simulations using ERA5 profiles and is estimated to contribute a standard deviation of approximately 0.5 m at 1° elevation, decreasing to below 0.2 m above 10°, corresponding to relative errors of 1% or less (Zus et al. 2012).

The uncertainty related to the surface level comes from residual biases or unmodeled errors in the onboard correction using the digital elevation model. A conservative 0.5 m surface height uncertainty translates to an increasing delay error with elevation, contributing more significantly at higher elevation angles due to the steeper signal geometry.

As shown in Fig. 8, the overall uncertainty budget is dominated by the fitting process. While PRETTY offers a higher delay resolution compared to previous missions, the quantization of the Delay Map still imposes limitations on tracking precision.

3.3 Estimation of chapman parameters from GNSS-R relative ionospheric delay

As the estimations of the relative ionospheric delay have demonstrated the capability to capture the first-order ionospheric effects with good agreement, a further step involves the inversion of Chapman layer parameters from the reflectometry-based ionospheric delay estimates. The goal is to retrieve information about the vertical structure of the ionosphere.

The Chapman layer function (Chapman 1931) models the electron density N_e as a function of altitude h providing a representation of the ionospheric F-layer. This model helps to understand how ionospheric conditions influence GNSS signal propagation at different altitudes.

The electron density profile as a function of height h is described by the following expression:

$$N_{\mathrm{e}}(h) = N_0 \cdot \exp\left(\frac{1}{2} * \left(1 - \left(\frac{h - h_m}{H}\right) - \exp\left(-\frac{h - h_{\mathrm{m}}}{H}\right)\right)\right) \tag{4}$$

where N_0 represents the peak electron density of the F-layer, h_{m} is the height of the F-Layer peak, and H represents the scale height.

The objective of the inversion is to determine the set of Chapman parameters h_m, N_0 and H that best reproduce the observed GNSS-R relative ionospheric delays. For each set of parameters, the electron density is computed along the ray point heights derived from the direct, incident, and reflected paths. These values are then integrated to calculate the Chapman-based sTEC per ray, from which the modeled relative ionospheric delay is obtained.

To fit the model to the observations, a cost function is defined as the root mean square error (RMSE) that minimizes the difference between the GNSS-R-derived ionospheric delay estimates and the Chapman-modeled delays:

$$\mathrm{RMSE} = \sqrt{\frac{1}{N}} \sum_i \left(\Delta_{\mathrm{p}_{iono}(\mathrm{obs}),\, i} - \Delta_{\mathrm{p}_{iono}(\mathrm{chp}),\, i}(h_\mathrm{m},\ N_0,\ H) \right)^2 \tag{5}$$

Here, $\Delta_{\mathrm{piono(obs)}}$ represents the GNSS-R-based relative ionospheric delay estimates, and $\Delta_{\mathrm{piono(chp)}}$ is the corresponding delay computed using the Chapman model for a given parameter set.

The inversion is carried out using a constrained optimization procedure, with the following parameter bounds: $h_\mathrm{m} \in [150, 450]$ km, $N_0 \in [1\mathrm{e}11, 1.5\mathrm{e}12]$ el/m^3, and $H \in [30, 150]$ km, based on Cushley et al. (2017).

The comparison between the GNSS-R-derived relative ionospheric delay estimates and the Chapman model fits is presented in Fig. 9. The blue curve shows the GNSS-R-based ionospheric delay estimation, while the red-dashed curve represents the Chapman delay computed using the fitted parameters.

The results show a strong agreement between the GNSS-R observations, and the Chapman model estimates across all events. The Chapman fits successfully capture the overall shape and magnitude of the relative ionospheric delay, including the location of the local minima typically observed between 2° and 4° of elevation. In most cases, the fitting reproduces both the curvature and the steep increase in delay at lower elevations, which is primarily driven by the longer ionospheric path lengths and increased sensitivity to the F-layer structure.

Some slight discrepancies are observed near the lowest elevations, where the GNSS-R estimations show more rapid changes than the Chapman model. This could be attributed to local ionospheric irregularities, the influence of the E-layer (the lower the elevation, the tangent point can fall below the F-layer), and limitations in resolving fine vertical structure using a simplified Chapman formulation.

Overall, the inversion demonstrates that GNSS-R code delay observations at grazing angles are capable of retrieving ionospheric vertical profile characteristics consistent with the classical Chapman layer model.

The fitted Chapman layer parameters for each event are summarized in Table 3. The fitting results demonstrate stable retrievals across the six events, with h_m ranging from approximately 307 to 361 km and.

H varying between 100 and 126 km. These values are in agreement with typical F-layer parameters reported in high-latitude regions under conditions of high solar activity (Bilitza et al. 2011).

The RMSE values of the fits remain below 1.7 m for all cases, indicating good consistency between the GNSS-R-derived ionospheric delay and the Chapman model reconstructions. The highest RMSE (1.66 m) corresponds to the 16 July event, which also had the highest solar flux level (F10.7 = 242), potentially reflecting enhanced ionospheric variability that is not fully captured by the smooth analytical Chapman model.

The retrieved F-layer peak heights (h_m) from GNSS-R observations are compared with ionosonde and EISCAT measurements reported in the global Ionospheric radio observatory (GIRO) database (Reinisch and Galkin 2011). The GIRO database provides access to ionograms from ionosonde and incoherent scatter radar stations, which probe the ionosphere to derive electron density profiles and associated parameters, including the F-layer peak height. For comparison, three stations located near the analyzed GNSS-R events were selected: two stations in Tromsø, northern Scandinavia—TROMSØ (URSI code TR169), EISCAT TROMSØ (TR170), and THULE (THJ76) in Greenland. Table 4 presents a comparison between the GNSS-R-derived h_m estimates (in kilometers) and those reported by the GIRO database.

The results show that the GNSS-R retrieved F-layer peak heights are generally in good agreement with those reported by nearby ionosonde and EISCAT stations. For most events, the differences between the estimates and the reference values remain within ± 15 km, which is consistent with expected spatial and temporal variations in the ionosphere. Notably, the event on July 28 exhibits the highest retrieved peak value (361.29 km), closely matched by EISCAT TROMSØ (TR170) at 350.60 km, suggesting enhanced ionospheric activity under elevated solar flux conditions. The largest discrepancies, such as the difference between the GNSS-R estimate and THJ76 on July 28, may be attributed to dynamic ionospheric conditions that introduce localized variability, spatial separation between the GNSS-R events and the ground-based stations, as well as limitations in model resolution or temporal collocation.

While the F-layer peak height h_m retrieved from the Chapman inversion provides valuable insight into the vertical ionospheric structure, further analysis is necessary to assess the horizontal consistency of this estimation across the GNSS-R geometry. In particular, the horizontal separation between the peak electron density points of the incident

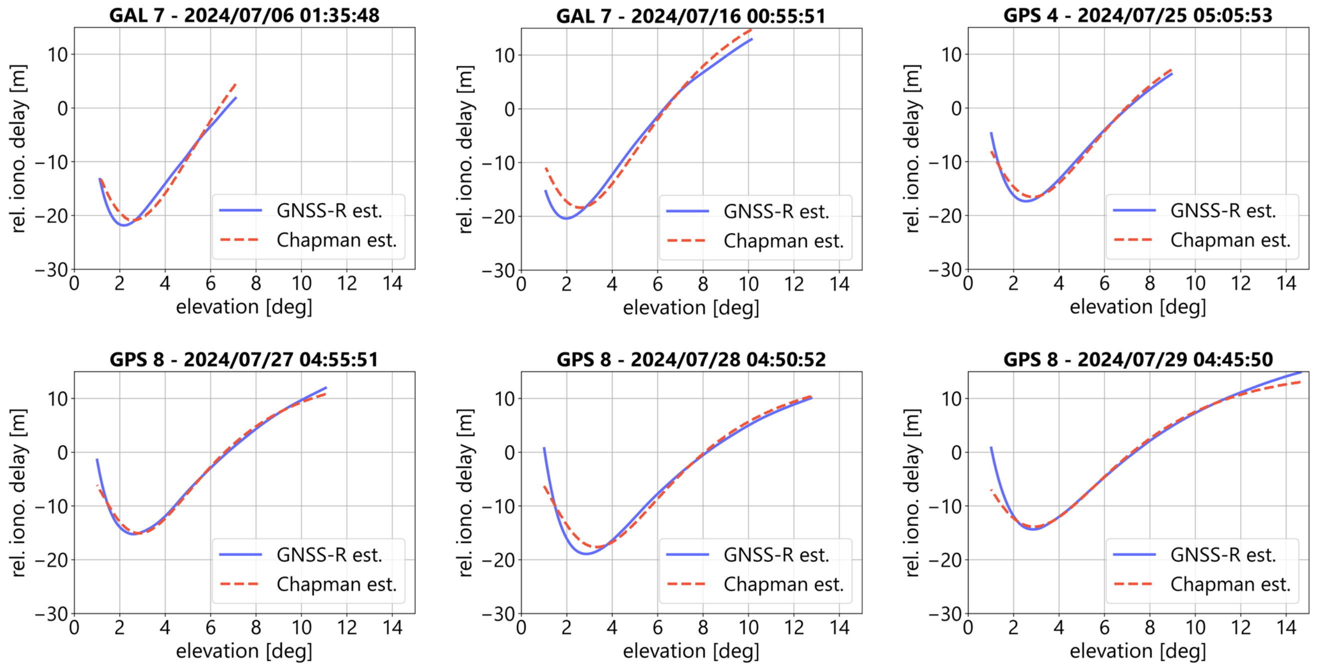

Fig. 9 Comparison between GNSS-R-derived relative ionospheric delay estimates from PRETTY observations (blue) and Chapman model estimations (red dashed) for six events in July 2024

Table 3 Retrieved Chapman layer parameters for each analyzed event, including the h_m, N_0, H, and the RMSE between the GNSS-R estimated and Chapman-modeled relative ionospheric delays

Date	GNSS-PRN	UTC	h_m [km]	N_0 [el/m^3]	H [km]	RMSE [m]
2024/07/06	GAL–7	01:35:48	315.71	5.35e11	123.48	1.47
2024/07/16	GAL–7	00:55:51	307.35	6.34e11	120.81	1.66
2024/07/25	GPS–4	05:05:53	323.26	4.33e11	115.22	0.83
2024/07/27	GPS–8	04:55:51	310.34	3.64e11	100.81	0.74
2024/07/28	GPS–8	04:50:52	361.29	4.09e11	111.61	1.31
2024/07/29	GPS–8	04:45:50	337.49	3.80e11	126.18	1.25

Table 4 F-layer peak height h_m (in km) retrieved from GNSS-R in comparison with stations from the GIRO database

Date	GNSS-PRN	UTC	GNSS-R	TR170	TR169	THJ76
2024/07/06	GAL–7	01:35:48	315.71	313.30	309.90	307.60
2024/07/16	GAL–7	00:55:51	307.35	ND	315.30	299.30
2024/07/25	GPS–4	05:05:53	323.26	318.50	307.50	294.10
2024/07/27	GPS–8	04:55:51	310.34	307.20	294.00	300.20
2024/07/28	GPS–8	04:50:52	361.29	350.60	327.50	306.30
2024/07/29	GPS–8	04:45:50	337.49	339.60	297.40	327.30

and reflected rays can span from approximately 2000 km at 14° elevation to over 3800 km at 1° elevation. This is relevant because such large distances imply that the two ray paths sample different regions of the ionosphere, where horizontal gradients and localized structures may influence the reliability of the inversion.

Figure 10 illustrates the relationship between the horizontal distance separating the h_m locations of the incident and reflected rays and the vertical difference in their respective peak heights. The data are color-coded by elevation angle and correspond to all six analyzed events. The h_m values are extracted from the NEDM2020 model as the altitude at which the maximum electron density occurs along each ray. From those peak points, the vertical height difference and geographic distance are computed.

Although the horizontal distances are considerable, the vertical differences in h_m remain within a relatively narrow

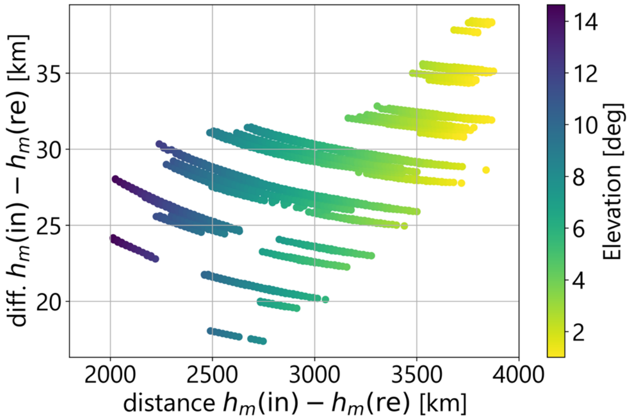

Fig. 10 Horizontal distance between the F-layer peak locations along the incident and reflected ray paths versus the corresponding vertical difference in peak height h_m

range of 18 to 37 km. This suggests that, despite the large separation between ionospheric penetration points, the retrieved h_m values are relatively stable, with limited vertical variability, partly because the climatological models used resolve rather smooth features. Nevertheless, the Chapman-based estimation of F-layer peak height can be reasonably interpreted as representative of the ionospheric structure along the GNSS-R track under the analyzed conditions, as further supported by the agreement with nearby ionosonde and EISCAT data.

3.4 Relative ionospheric delay cancelation point and the f-layer structure

In addition to the Chapman-based inversions, we identify a cancelation point in the relative ionospheric delay, defined as the elevation angle where the contributions from the direct and combined incident-reflected signal paths cancel out, resulting in a net delay of zero. This point is evident in Fig. 7 across all of the events, where the delay curve intersects the zero line. To explore the physical basis of this phenomenon, Chapman layer simulations are performed, varying the N_0 with values of 0.5e12 m^{-3}, 1.0e12 m^{-3}, and 1.5e12 m^{-3}, while assigning h_m values of 250 km, 300 km, and 350 km. The results of the different scenarios are presented in Fig. 11. The color-coded lines represent variations in the F-layer peak height, while the dashed line styles represent variations in peak electron density.

As shown in Fig. 11, there is a clear relationship between the elevation angle of the cancelation point and the F-layer peak height. For example, a cancelation point at approximately 6.83° elevation (July 06) corresponds to an h_m of 317 km, while a shift to 8.29° (July 28) aligns with an h_m of 367 km. Table 5 present the retrieved h_m using the cancelation point method. While some discrepancies remain, the results show good agreement with the h_m values obtained from Chapman-based fitting. These findings suggest that this cancelation point could serve as a proxy for estimating the F-layer peak height. Future work will further investigate its applicability, considering factors such as horizontal ionospheric gradients and the sensitivity to GNSS-R geometry.

4 Conclusions

This study demonstrates that, after accurately correcting for the tropospheric delay, it is possible to successfully estimate the first-order relative ionospheric delay using code delay observations at grazing angles from the ESA PRETTY mission. These findings highlight the potential of single-frequency GNSS-R missions like PRETTY to capture ionospheric delay effects accurately, even at very low-elevation angles, using model-based atmospheric corrections.

Thanks to PRETTY's extended observation capabilities down to 1° of elevation, we determined that the relative ionospheric delay reaches its maximum negative value at around 3°, averaging − 20 m across the six events analyzed in the North Pole region, with variations influenced by solar activity. This elevation coincides with the peak delay contribution from the direct signal, which accounts for approximately 60% of the total ionospheric delay at 3°, with the remaining 40% from the combined incident and reflected paths. At higher elevations (e.g., 10°), this proportion shifts, with the direct ray contributing only about 40%. This highlights that ionospheric effects, particularly from the direct signal path, must not be neglected in GNSS-R applications operating at low elevations, consistent with the conclusions of Camps et al. (2016).

The uncertainty analysis shows that the dominant source of error in the relative ionospheric delay estimation comes from the delay fitting process. While PRETTY offers improved delay resolution (~ 7.8 m) compared to previous missions, the discrete sampling of the Delay Map and the peak detection method lead to uncertainties of ± 2.6 m. Nevertheless, the exponential model used in the fitting process provides a high degree of confidence, with R^2 values near 1 for all events.

The uncertainty from the relative tropospheric delay correction is smaller, ranging from ~ 0.2 m at 15° to ~ 1 m at 1°, and the uncertainty due to surface level bias or unmodeled errors remains below ~ 0.25 m. These sources must be considered when interpreting delay estimates for the purpose of retrieving ionospheric parameters.

The application of a Chapman-based inversion to GNSS-R code delay observations shows promising potential for retrieving the vertical structure of the ionosphere. F-layer peak heights h_m estimated from the fitted Chapman model ranged from 307 to 367 km, in agreement with expected

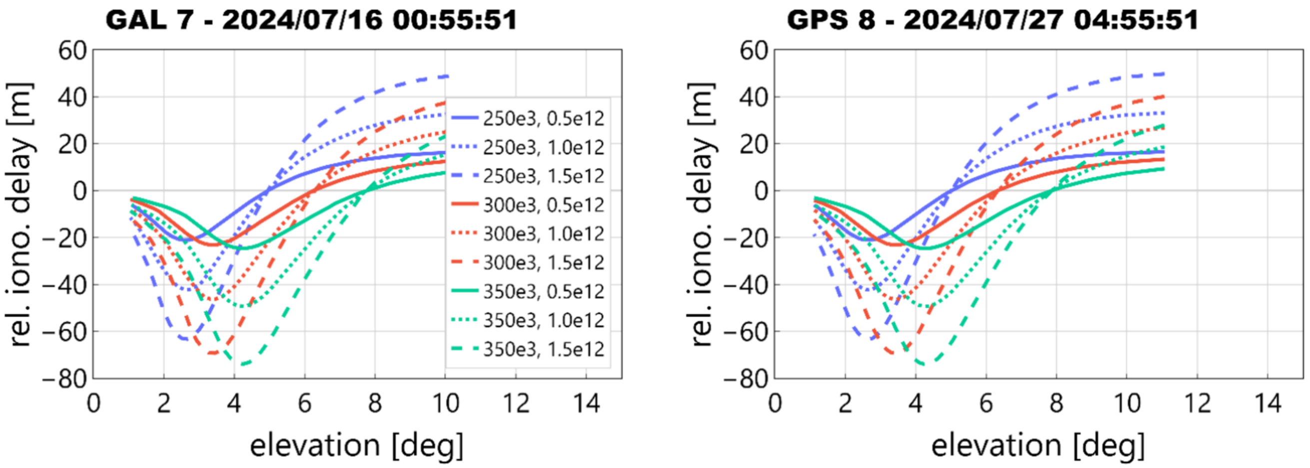

Fig. 11 Chapman layer simulation for the events of 16 and 27 July. Color-coded lines present variations in peak height (h_m), while dashed style indicates variations in peak electron density (N_0). The legend order is h_m, N_0

Table 5 Estimated F-layer peak heights derived from the elevation angle of the relative ionospheric delay cancelation point

Date	GNSS-PRN	UTC	Elevation. [deg]	h_m [km]
2024/07/06	GAL–7	01:35:48	6.83	317
2024/07/16	GAL–7	00:55:51	6.41	303
2024/07/25	GPS–4	05:05:53	7.20	330
2024/07/27	GPS–8	04:55:51	6.85	318
2024/07/28	GPS–8	04:50:52	8.29	367
2024/07/29	GPS–8	04:45:50	7.44	338

values for high-latitude regions under high solar activity conditions (F10.7 = 150–250). The inversion process yielded a mean RMSE of 1.2 m (approximately 4 TECU) across all analyzed events, indicating strong consistency between GNSS-R-derived ionospheric delay and the modeled Chapman reconstruction.

This concept of inverting Chapman parameters is similar to that applied in GNSS radio occultation (GNSS-RO) studies, such as (Elvidge et al. 2024), where a flexible Chapman function (Vary-Chap) was implemented within a one-dimensional variational framework to reconstruct electron density profiles from bending angle measurements.

While the observables and geometries differ, GNSS-R, relying on reflected code delays and GNSS-RO using limb-sounding bending angles, both techniques aim to retrieve key parameters of the ionospheric F-layer, namely, peak electron density (N_0), peak height (h_m), and scale height (H), through Chapman model fitting. These findings reinforce the notion that GNSS-R reflectometry is a valuable and complementary technique for ionospheric characterization, particularly in regions and conditions, such as polar or oceanic areas, where traditional ground-based methods are unavailable or limb-sounding techniques are limited.

Comparison with independent measurements from nearby ionosonde and EISCAT stations shows generally good agreement. For most events, the differences between the GNSS-R-derived h_m values and those reported by the ground-based stations remain within ± 15 km, which is within the expected range of spatial and temporal ionospheric variability. Smaller differences were observed with respect to the EISCAT TROMSØ (TR170) station, while larger discrepancies were noted when compared with THULE (THJ76), likely due to dynamic ionospheric conditions, increased spatial separation, or the lack of precise temporal collocation.

Accurate characterization and correction of ionospheric delays are essential for achieving high-precision positioning, satellite altimetry (including reflectometry), and atmospheric sounding. The results indicate that GNSS-R can retrieve first-order ionospheric delays at grazing angles and provide valuable input for multi-technique ionospheric studies, enhancing the understanding of the spatiotemporal behavior of the F-layer peak and electron density profiles. This work contributes to space geodesy by introducing an alternative technique for retrieving ionospheric parameters under challenging low-elevation geometries, potentially extending global ionospheric mapping capabilities beyond those offered by ground-based networks and radio occultation.

Future work could delve deeper into the relationship between the relative ionospheric delay cancelation point and the F-layer peak height, as well as assess the sensitivity of these estimations to GNSS-R geometry and horizontal ionospheric gradients. In addition, residual discrepancies between the estimated and modeled delays may also reveal second-order ionospheric effects, including geomagnetic effects. Once PRETTY's phase observables complete their ongoing verification and validation and become available to the scientific community, their combination with code observables could enable absolute TEC retrievals, further enhancing ionospheric characterization through GNSS-R reflectometry at grazing angles.

Acknowledgements The authors would like to thank Beyond Gravity Austria GmbH (BGA) for providing PRETTY data.

Author contribution Conceptualization, M.M., M.S., G.S., and F.Z.; methodology, M.M., M.S., and F.Z.; software, M.M., M.S., A.D., and F.Z.; data resources, M.M., M.S., F.Z., and A.D.; writing—original draft preparation, M.M.; writing—review and editing, M.M., M.S., F.Z., G.S., A.D., M.H., J.W., and H.N.; visualization, M.M.; supervision, M.S., J.W., and M.H.

Funding Open Access funding enabled and organized by Projekt DEAL.

Data availability Data are available upon reasonable request from the corresponding author and under the authorization of BGA.

Declarations

Conflict of interest The authors declare no conflict of interest.

References

AlonsoArroyo A, Zavorotny VU, Camps A (2016) Sea ice detection using GNSS-R data from UK TDS-1. IEEE Int Geosci Remote Sens Symp (IGARSS) 2016:2001–2004. https://doi.org/10.1109/IGARSS.2016.7729516

Bilitza D, McKinnell L-A, Reinisch B, Fuller-Rowell T (2011) The international reference ionosphere today and in the future. J Geodesy 85(12):909–920. https://doi.org/10.1007/s00190-010-0427-x

Bilitza D, Pezzopane M, Truhlik V, Altadill D, Reinisch BW, Pignalberi A (2022) The international reference ionosphere model: a review and description of an ionospheric benchmark. Rev Geophys. https://doi.org/10.1029/2022RG000792

Camps A, Park H, Foti G, Gommenginger C (2016) ionospheric effects in GNSS-Reflectometry from space. IEEE J Sel Top Appl Earth Obs Remote Sens. https://doi.org/10.1109/JSTARS.2016.2612542

Cardellach E, Ao CO, de la Torre Juárez M, Hajj GA (2004) Carrier phase delay altimetry with GPS-reflection/occultation interferometry from low Earth orbiters. Geophys Res Lett. https://doi.org/10.1029/2004GL019775

Cardellach E, Wickert J, Baggen R, Benito J, Camps A, Catarino N, Chapron B, Dielacher A, Fabra F, Flato G, Fragner H, Gabarró C, Gommenginger C, Haas C, Healy S, Hernandez-Pajares M, Høeg P, JäGgi A, Kainulainen J, Zuffada C (2018) GNSS transpolar earth reflectometry exploriNg system (G-TERN): mission concept. IEEE Access 6:13980–14018. https://doi.org/10.1109/ACCESS.2018.2814072

Cardellach E, Li W, Rius A, Semmling M, Wickert J, Zus F, Ruf CS, Buontempo C (2020) First precise spaceborne sea surface altimetry with gnss reflected signals. IEEE J Sel Topics Appl Earth Obs Remote Sens 13:102–112. https://doi.org/10.1109/JSTARS.2019.2952694

Cartwright J, Banks CJ, Srokosz M (2019) Sea Ice detection using GNSS-R data from TechDemoSat-1. J Geophys Res: Oceans 124(8):5801–5810. https://doi.org/10.1029/2019JC015327

Chapman S (1931) The absorption and dissociative or ionizing effect of monochromatic radiation in an atmosphere on a rotating earth part II Grazing incidence. Proc Phys Soc 43(5):483. https://doi.org/10.1088/0959-5309/43/5/302

Cushley AC, Kabin K, Noël J-M (2017) Faraday rotation of automatic dependent surveillance-broadcast (ADS-B) signals as a method of ionospheric characterization. Radio Sci 52(10):1293–1300. https://doi.org/10.1002/2017RS006319

Dielacher A, Fragner H, Koudelka O (2022) PRETTY: passive GNSS-reflectometry for CubeSats. E & i Elektrotech Informationstech 139(1):25–32. https://doi.org/10.1007/s00502-022-00993-7

Elvidge S, Healy SB, Culverwell ID (2024) One-dimensional variational ionospheric retrieval using radio occultation bending angles: 2. validation. Sp Weather. https://doi.org/10.1029/2023SW003571

Fabra F, Cardellach E, Rius A, Ribo S, Oliveras S, Nogues-Correig O, Belmonte Rivas M, Semmling M, D'Addio S (2011) Phase altimetry with dual polarization GNSS-R over sea ice. IEEE Trans Geosci Remote Sens 50(6):2112–2121. https://doi.org/10.1109/TGRS.2011.2172797

Foti G, Gommenginger C, Jales P, Unwin M, Shaw A, Robertson C, Roselló J (2015) Spaceborne GNSS reflectometry for ocean winds: first results from the UK TechDemoSat-1 mission. Geophys Res Lett 42(13):5435–5441. https://doi.org/10.1002/2015GL064204

Hersbach H, Bell B, Berrisford P, Hirahara S, Horányi A, Muñoz-Sabater J, Nicolas J, Peubey C, Radu R, Schepers D, Simmons A, Soci C, Abdalla S, Abellan X, Balsamo G, Bechtold P, Biavati G, Bidlot J, Bonavita M, Thépaut J (2020) The ERA5 global reanalysis. Q J R Meteorol Soc 146(730):1999–2049. https://doi.org/10.1002/qj.3803

Hofmann-Wellenhof B, Lichtenegger H, Collins J (2012) Global positioning system: theory and practice. Springer Science & Business Media, Germany

Hoque MM, Jakowski N, Prol FS (2022) A new climatological electron density model for supporting space weather services. J Sp Weather Sp Clim 12:1. https://doi.org/10.1051/swsc/2021044

Moreno M, Semmling M, Stienne G, Hoque M, Wickert J (2023) Characterizing ionospheric effects on gnss reflectometry at grazing angles from space. Remote Sens. https://doi.org/10.3390/rs15205049

Morton YJ, Yang Z, Breitsch B, Bourne H, Rino C (2020) Ionospheric Effects, Monitoring, and Mitigation Techniques. In Position, Navigation, and Timing Technologies in the 21st Century (pp. 879–937). John Wiley & Sons, Ltd. https://doi.org/10.1002/9781119458449.ch31

Nava B, Coïsson P, Radicella SM (2008) A new version of the NeQuick ionosphere electron density model. J Atmos Solar Terr Phys 70(15):1856–1862. https://doi.org/10.1016/j.jastp.2008.01.015

Reinisch BW, Galkin IA (2011) Global ionospheric radio observatory (GIRO). Earth, Planets Space,. https://doi.org/10.5047/eps.2011.03.001

Ren X, Liu H, Zhang J, Mei D, Zhang X (2022) An improved method for ionospheric TEC estimation using the spaceborne GNSS-R observations. IEEE Trans Geosci Remote Sens 60:1–12. https://doi.org/10.1109/TGRS.2022.3192983

Rius A, Cardellach E, Fabra F, Li W, Ribó S, Hernández-Pajares M (2017) Feasibility of GNSS-R ice sheet altimetry in greenland using TDS-1. Remote Sens. https://doi.org/10.3390/rs9070742

Ruf C, Gleason S, Jelenak Z, Katzberg S, Ridley A, Rose R, Scherrer J, Zavorotny V (2013a) The NASA EV-2 cyclone global navigation satellite system (CYGNSS) mission. IEEE Aerosp Conf 2013:1–7. https://doi.org/10.1109/AERO.2013.6497202

Ruf C, Unwin M, Dickinson J, Rose R, Rose D, Vincent M, Lyons A (2013b) CYGNSS: enabling the future of hurricane prediction [Remote Sensing Satellites]. IEEE Geosci Remote Sens Mag 1(2):52–67. https://doi.org/10.1109/MGRS.2013.2260911

Semmling AM, Leister V, Saynisch J, Zus F, Heise S, Wickert J (2016) A phase-altimetric simulator: studying the sensitivity of earth-reflected gnss signals to ocean topography. IEEE Trans Geosci Remote Sens 54(11):6791–6802. https://doi.org/10.1109/TGRS.2016.2591065

Unwin M, Jales P, Tye J, Gommenginger C, Foti G, Rosello J (2016) Spaceborne GNSS-reflectometry on techDemoSat-1: early mission operations and exploitation. IEEE J Sel Top Appl Earth Obs Remote Sens 9(10):4525–4539. https://doi.org/10.1109/JSTARS.2016.2603846

Wang Y, Morton YJ (2022) Ionospheric total electron content and disturbance observations from space-borne coherent GNSS-R measurements. IEEE Trans on Geosci Remote Sens 60:1–13. https://doi.org/10.1109/TGRS.2021.3093328

Wang Y (2023a) Ionosphere TEC Observation Over Ocean Using Single-Frequency Wideband GNSS Signal Reflectometry. Proceedings of the 36th International Technical Meeting of the Satellite Division of The Institute of Navigation (ION GNSS+ 2023). 3941–3946. https://doi.org/10.33012/2023.19415

Wang Y (2023b) Troposphere sensing using grazing-angle GNSS-R measurement from LEO satellites. Geophys Res Lett. https://doi.org/10.1029/2023GL106249

Xing J, Datta-Barua S, Garrison J, Ridley A, Pervan B (2015) Relative ionospheric ranging delay in LEO GNSS oceanic reflections. IEEE Geosci Remote Sens Lett 12(7):1416–1420. https://doi.org/10.1109/LGRS.2015.2404912

Zus F, Bender M, Deng Z, Dick G, Heise S, Shang-Guan M, Wickert J (2012) A methodology to compute GPS slant total delays in a numerical weather model. Radio Sci. https://doi.org/10.1029/2011RS004853